JOURNAL OF THERMOPHYSICS AND HEAT TRANSFER
Vol. 8, No. 4, Oct.–Dec. 1994

# Strongly Coupled Radiative Transfer and Joule Heating in an Arc Heater Cathode

P. Durgapal* and Grant Palmer†
*NASA Ames Research Center, Moffett Field, California 94035*

**Radiation and Joule heating in the electrode region of an arc heater are discussed. Radiative transport equations for a true axisymmetric geometry are used. A subsonic code is developed to numerically solve the fluid equations with strongly coupled radiation, $\nabla \cdot q_r$ and Joule heating $j \cdot E$, representative of a high-pressure and high-current arc heater. Analytic expression for the divergence of radiative heat flux derived in a previous paper is used. Jacobians of the radiation term are derived. The Joule heating term is computed using a previously developed code. The equilibrium gas model consists of seven species. The fluxes are differenced using Van Leer flux splitting. Using this code the effects of radiative cooling on the thermodynamic parameters of the arc core are discussed.**

## Nomenclature

$A$ = absorption coefficient $A(r)$
$A'$ = absorption coefficient $A(r')$
$A_x$ = absorption coefficient $A(rx)$
$B$ = Planck's distribution function
$c$ = speed of sound, m/s
$c_\infty$ = freestream speed of sound, m/s
$\boldsymbol{E}$ = electric field vector, V/m
$e$ = total energy, J/m$^3$
$\boldsymbol{F}, \boldsymbol{G}, \boldsymbol{H}$ = inviscid flux vectors in axisymmetric geometry
$\hat{\boldsymbol{F}}, \hat{\boldsymbol{G}}, \hat{\boldsymbol{H}}$ = inviscid flux vectors in generalized coordinates
$\mathcal{J}$ = identity matrix
$I(R)$ = radiative intensity at the wall
$j$ = current density, A/m$^2$
$p$ = pressure
$q_k$ = conductive heat flux
$q_r$ = radiative heat flux in the radial direction
$q_z$ = radiative heat flux in the streamwise direction
$R$ = inner radius of the electrode, m
$Re$ = freestream Reynolds number
$r$ = radial coordinate direction
$r', x$ = integration variables
$\boldsymbol{U}, \boldsymbol{S}, \boldsymbol{V}$ = viscous flux vectors in axisymmetric geometry
$\hat{\boldsymbol{U}}, \hat{\boldsymbol{S}}, \hat{\boldsymbol{V}}$ = viscous flux vectors in generalized coordinates
$u$ = velocity component in streamwise direction
$v$ = velocity component in radial direction
$z$ = streamwise coordinate direction
$\Delta t$ = time step
$\varepsilon$ = emissivity of the wall
$\eta$ = reflectivity of the wall
$\nu$ = frequency
$\xi, \zeta$ = generalized coordinates
$\rho$ = density, kg/m$^3$
$\rho_\infty$ = freestream density, kg/m$^3$
$\tau_{ij}$ = stress tensor

Presented as Paper 93-2801 at the AIAA 28th Thermophysics Conference, Orlando, FL, July 6–9, 1993; received Aug. 20, 1993; revision received March 23, 1994; accepted for publication April 4, 1994. 

*Research Scientist, Thermosciences Institute, M/S 229-4. Member AIAA.
†Research Scientist, Thermosciences Institute, M/S 230/2. Member AIAA.

## I. Introduction

ARC heaters are complex devices that have widespread application in the aerospace field. The primary use of these facilities is to simulate the thermal environmental conditions encountered by fast re-entry vehicles for material testing. The current arcjet facilities at Ames Research Center were designed to simulate entry from near Earth orbit (Space Shuttle) and to simulate entry into the atmosphere of the giant planets (Galileo probe). In recent years there has been increased interest in planetary missions. Return missions will involve entry into the Earth's atmosphere at velocities substantially greater than the entry velocities experienced by the Space Shuttle. High enthalpy and high-pressure arcjets are needed to simulate and characterize heat shield materials for an entering planetary spacecraft. The development of such highly energetic advanced capability requires improved arcjet technology and better understanding of the physics of arcs encountered in different regions of the arc heater. The main problems encountered in the design of an arc heater are arc control, downstream electrode (cathode) erosion, and radiation loss. This study is part of an ongoing research at NASA Ames to construct a physical model in a step-by-step manner. This model will be used to simulate high enthalpy flows for material testing. The final model will be used to design future arcjets. The electrode region of an arc heater has not previously been the subject of any systematic study.

At high temperatures radiative energy transfer becomes an important mode of heat transfer together with conduction and convection. Due to high current, this region is characterized by a strong Joule heating term in the energy equation. For these conditions the energy equation of the flowfield must include the Joule heating term $\boldsymbol{j} \cdot \boldsymbol{E}$, together with the radiation term. The electrical characteristics for high-pressure, high-current arcs in the downstream cathode region of an arc heater were discussed in two previous papers.[1,2] In another paper,[3] an expression for the radiative heat flux was derived assuming a gray wall. In the energy equation contribution of the radiative transfer occurs as the expression for the divergence of the heat flux vector $\boldsymbol{q}_r$. An expression for the $\nabla \cdot \boldsymbol{q}_r$ was derived analytically for axisymmetric flow.[3]

In this article, computational equations for the flowfield in the downstream cathode region of an arc heater are derived.

The code developed is subsonic and is representative of the true flow in the downstream cathode region. It includes a radiation term and a Joule heating term. The code treats the radiation term implicitly. The Joule heating term is treated explicitly in the present work. It is computed using a previously developed electromagnetic code.[1] The Jacobian of the radiative source term with respect to the species number densities is computed analytically using the same techniques that were used in the derivation of the divergence of $q_r$. The Jacobian with respect to the temperature is computed numerically. The resulting set of nonlinear equations is solved using a time-marching scheme for an axisymmetric problem.

In the first part of this article the basic equations needed to describe the subsonic flow in the electrode region are described. These, together with the necessary boundary conditions, are then solved numerically. Results are presented in Sec. III. Temperature distribution and the corresponding radiative heat flux profile for a downstream cathode region are discussed. This is done for two cases: 1) electrode with adiabatic wall, and 2) electrode with cooled wall. The enthalpy distribution for the two cases is also discussed.

## II. Theory

The main features of an arc heater are shown in the upper part of Fig. 1. It consists of an upstream electrode, a constrictor column, and a downstream electrode with flow in the direction shown. For the present work the region of interest is the downstream electrode, which is assumed to be a cathode. Details of the cathode region are shown in the middle part of Fig. 1. In general there are 2–8 electrodes in the cathode assembly. In the figure insulators and electrodes are shown flat and curved just to distinguish one from the other. In reality both have similar shape and the same i.d. The arc that enters the cathode region from the constrictor column is characterized by an intense core of high-current density and high temperature. At each electrode ring, the arc terminates as an arc foot. Input energy is provided by Joule heating. Because of Joule heating in the arc core the temperature of the gas rises, leading to strong radiative emission. This emission travels through the surrounding gas to the electrode wall as depicted in the lower part of Fig. 1. In order to keep the electrode wall temperature below an acceptable level, it is water cooled.

In a previous paper[3] an expression for the divergence of the radiative heat flux for an axisymmetric geometry was computed. In this article the radiative term is treated implicitly. For this treatment the Jacobian of the radiative source term

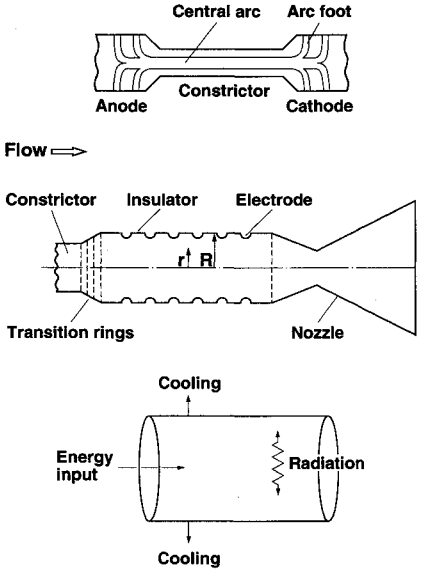


**Fig. 1 Electrode environment of an arc heater.**

with respect to the temperature and density is needed. The expression for the Jacobian with respect to the density is computed using the techniques discussed in Ref. 3. The Jacobian with respect to temperature is computed numerically.

### A. Governing Equations

The governing equations are the axisymmetric Navier-Stokes equations for an equilibrium reacting gas.[4] Expressed in vector form they are

$$\frac{\partial \boldsymbol{Q}}{\partial t} + \frac{\partial \boldsymbol{F}}{\partial z} + \frac{\partial \boldsymbol{G}}{\partial r} + \frac{\boldsymbol{H}}{r} = \frac{1}{Re}\left(\frac{\partial \boldsymbol{U}}{\partial z} + \frac{\partial \boldsymbol{S}}{\partial r} + \frac{\boldsymbol{V}}{r} + \boldsymbol{W}\right) \tag{1}$$

where

$$\begin{aligned}
\boldsymbol{Q} &= [\rho, \rho u, \rho v, e]^T \\
\boldsymbol{F} &= [\rho u, \rho u^2 + p, \rho uv, (e + p)u]^T \\
\boldsymbol{G} &= [\rho v, \rho uv, \rho v^2 + p, (e + p)v]^T \\
\boldsymbol{H} &= [\rho v, \rho uv, \rho v^2, (e + p)v]^T \\
\boldsymbol{U} &= (0, \tau_{zz}, \tau_{zr}, -q_z + u\tau_{zz} + v\tau_{zr})^T \\
\boldsymbol{S} &= (0, \tau_{zr}, \tau_{rr}, -q_r + u\tau_{zr} + v\tau_{rr})^T \\
\boldsymbol{V} &= (0, \tau_{zr}, \tau_{rr} - \tau_{\theta\theta}, -q_r + u\tau_{zr} + v\tau_{rr})^T \\
\boldsymbol{W} &= (0, 0, 0, \nabla\cdot\boldsymbol{q}_r - \boldsymbol{j}\cdot\boldsymbol{E})^T
\end{aligned} \tag{2}$$

The source terms $\boldsymbol{W}$ include the radiation term $\nabla\cdot\boldsymbol{q}_r$ and the Joule heating term $\boldsymbol{j}\cdot\boldsymbol{E}$. In a previous paper[3] an expression for the radiative heat flux was derived for an absorbing and emitting gas contained in a cylinder whose internal surface is gray

$$\begin{aligned}
q(r) = {} & \pi I(R)\int_0^1 dx\, \exp(-bA\sqrt{R^2 - r^2x^2})(Y_1 - Y_2) \\
& + \pi\int_0^1 dx\, Y_1\int_{rx}^R dr'\, \frac{bA'r'B(r')}{\sqrt{r'^2 - r^2x^2}}\, Y_3 \\
& + \pi\int_0^1 dx\, Y_1\int_{rx}^r dr'\, \frac{bA'r'B(r')}{\sqrt{r'^2 - r^2x^2}}\, Y_4 \\
& - \pi\int_0^1 dx\, Y_2\int_r^R dr'\, \frac{bA'r'B(r')}{\sqrt{r'^2 - r^2x^2}}\, Y_3
\end{aligned} \tag{3}$$

Here, the radiative intensity at the wall $I(R) = [\varepsilon B(R) + \eta q(R)]/\pi$. The emissivity $\varepsilon$ and reflectivity $\eta$ of the wall satisfy the relation $\varepsilon + \eta = 1.0$. Also, $Y_1 = \exp(-bAr\sqrt{1 - x^2})$, $Y_2 = \exp(bAr\sqrt{1 - x^2})$, $Y_3 = \exp(-bA\sqrt{r'^2 - r^2x^2})$, and $Y_4 = \exp(bA\sqrt{r'^2 - r^2x^2})$. The expression for the radiative heat flux at the wall is given by

$$\begin{aligned}
q(R) = {} & \frac{1}{1 + \eta(1 - Y)}\Bigg[\varepsilon B(R)(Y - 1) \\
& + \pi\int_0^1 dx\, Y_{1R}\int_{Rx}^R dr'\, \frac{bA'r'B(r')}{\sqrt{r'^2 - R^2x^2}}\,(Y_{3R} + Y_{4R})\Bigg]
\end{aligned} \tag{4}$$

where $Y = \int_0^1 dx\, \exp(-2bAR\sqrt{1 - x^2})$, and $Y_{1R}$, $Y_{3R}$ and $Y_{4R}$ are the functions $Y_1$, $Y_3$, and $Y_4$ evaluated at $r = R$, respectively. In all these equations $A$ is the absorption coefficient. The contribution of the radiation term appears as the divergence of the radiation heat flux vector. In cylindrical coordinates the divergence of the radiative flux has the form

$$\nabla\cdot\boldsymbol{q}_r = \frac{dq_r}{dr} + \frac{q_r}{r} \tag{5}$$

The expression for the $\nabla \cdot q_r$ was derived analytically for axisymmetric flow[3] and is given by

$$\nabla \cdot q_r = \pi \int_0^1 dx \left\{ I(R) \exp(-bA\sqrt{R^2 - r^2x^2}) \left[ \frac{(Y_1 - Y_2)}{r} + \frac{bArx^2(Y_1 - Y_2)}{\sqrt{R^2 - r^2x^2}} - bA\sqrt{1 - x^2}(Y_1 + Y_2) \right] + b \left[ \frac{B(r)A}{\sqrt{1 - x^2}} - \frac{B(rx)A_x}{\sqrt{1 - x^2}} \right] (Y_1^2 + 1) + bA_xB(rx)\sqrt{1 - x^2}(Y_1^2 + 1) - \frac{bAB(r)(Y_1^2 - 1)}{\sqrt{1 - x^2}} \right\} + \pi \int_0^1 dx \left\{ \frac{Y_1}{r}(1 - bAr\sqrt{1 - x^2}) \int_{rx}^r dr' \times \frac{bA'r'B(r')}{\sqrt{r'^2 - r^2x^2}}(Y_3 + Y_4) + rx^2Y_1 \int_{rx}^r dr'br' \times \left[ \frac{B(r')A'}{(r'^2 - r^2x^2)^{3/2}} - \frac{B(rx)A_x}{(r'^2 - r^2x^2)^{3/2}} \right] (Y_3 + Y_4) + bArx^2Y_1 \int_{rx}^r dr'br' \left[ \frac{B(r')A'}{(r'^2 - r^2x^2)} - \frac{B(rx)A_x}{(r'^2 - r^2x^2)} \right] (Y_3 - Y_4) \right\} + \pi \int_0^1 dx \left\{ \frac{1}{r} \left[ (Y_1 - Y_2) - bAr\sqrt{1 - x^2}(Y_1 + Y_2) \right] \int_r^R dr' \frac{bA'r'B(r')}{\sqrt{r'^2 - r^2x^2}} Y_3 + bArx^2(Y_1 - Y_2) \int_r^R dr' \frac{bA'r'B(r')}{r'^2 - r^2x^2} Y_3 + rx^2(Y_1 - Y_2) \int_r^R dr' \frac{bA'r'B(r')}{(r'^2 - r^2x^2)^{3/2}} Y_3 \right\} \quad (6)$$

In Ref. 3 the radiation term was coupled explicitly. In this article, the radiation term is evaluated implicitly. This means that we need partial derivatives of $\nabla \cdot q_r$ with respect to the species densities and the temperature. The partial derivatives with respect to the species densities are computed by exact differentiation using the techniques discussed in Ref. 3. The derivative with respect to the temperature is computed numerically. The values of $\nabla \cdot q_r$ are computed from the exact expression given in Eq. (6). Treating the radiation term implicitly increases the computational cost of the algorithm, but enhances numerical stability. The Joule heating term is computed using a previously developed electromagnetic code.[1,2]

The equations are transformed into a generalized $\xi$, $\zeta$ coordinate system. Placed into delta form representing the explicit Euler time march scheme, the solution algorithm becomes

$$\left( \mathcal{J} - \Delta t \frac{\partial \hat{W}}{\partial \hat{Q}} \right) \delta \hat{Q} = -\Delta t \left[ \delta_\xi \hat{F} + \delta_\zeta \hat{G} + \frac{\hat{H}}{r} - \frac{1}{Re} \left( \delta_\xi \hat{U} + \delta_\zeta \hat{S} + \frac{\hat{V}}{r} \right) - \hat{W} \right] \quad (7)$$

In Eq. (7)

$$\delta \hat{Q} = (Q^{n+1} - Q^n)/J$$

$$\hat{F} = (\xi_z F + \xi_r G)/J$$

$$\hat{G} = (\zeta_z F + \zeta_r G)/J$$

$$\hat{U} = (\xi_z u + \xi_r S)/J$$

$$\hat{S} = (\zeta_z U + \zeta_r S)/J$$

$$\hat{H} = H/J \qquad \hat{V} = V/J \qquad \hat{W} = W/J$$

In Eq. (7) the term $\delta_\xi \hat{F}$ represents $\partial \hat{F}/\partial \xi$ and $\delta_\zeta \hat{G}$ represents $\partial \hat{G}/\partial \zeta$. The superscript $n$ indicates the current time step and, $n + 1$, the next time level. The transformation Jacobian $J$ is given by

$$J = \xi_z \zeta_r - \xi_r \zeta_z$$

The inviscid fluxes in Eq. (7) are differenced using Van Leer flux vector splitting.[5] These methods are called upwind differencing techniques because they split the fluxes into positive and negative components based on the direction of signal propagation. MUSCL[6] differencing is used to achieve second-order spatial accuracy. The chemical composition of the gas is obtained by minimizing Gibbs free energy while maintaining constant pressure and enthalpy. The minimization is performed via Newton-Raphson iteration, yielding updated values of species mole fractions, temperature, and total energy.

### B. Boundary Conditions

Subsonic boundary conditions are imposed on both the inflow and outflow boundaries. Along subsonic boundary lines, three of the eigenvalues, $u$, $u$, $u + c$, are positive. The fourth eigenvalue, $u - c$, is negative. Along the inflow line, total pressure, total temperature, and the velocity component $v$ are specified. The velocity component $u$ is obtained by solving the characteristic relation

$$u^{n+1} - u^n = \frac{-\lambda_4(\Delta p - \rho c \Delta u)}{(1 - \lambda_4)\left( \frac{\partial p}{\partial u} - \rho c \right)} \quad (8)$$

where $\lambda_4 = u - c$. In Eq. (8), the symbol $\Delta$ indicates a spatial difference. Along the outflow line, pressure is held fixed at the freestream pressure. The other quantities are extrapolated from the interior.

In the computation of the Joule heating term the following boundary conditions and subsidiary conditions that are characteristic of the electrode region were applied on the electrode surface and the insulating wall. They are as follows:

1) On the surface of the electrode (good conductor), tangential component of the electric field vanishes.

2) On the insulating wall, normal component of the current is zero.

3) The current that runs through an arbitrary surface, crossing the flow ahead of the electrodes, is equal to the load current.

4) The electrodes are ballasted to share the current equally.

5) Since all the current is forced to terminate on the electrodes, the stream functions corresponding to the last axial point are zero.

## III. Results

In the present study thermodynamic parameters together with the radiative heat flux are computed for the downstream cathode region of an arc heater. A finite difference algorithm with subsonic equilibrium boundary conditions is used for this purpose. A strongly coupled radiation term is used in the energy equation. An electrode assembly with two electrodes was chosen for computations. The electrodes are separated by an insulator. Also, there are insulators at the beginning and end of the electrode assembly. The inner radius of the electrode is 5.2 cm. The cylindrical cathode region of constant radius $R$ is discretized using a 39 × 39 grid. Computations are done for a cold wall ($T_w$ = 3157 K) and an adiabatic wall. The expression for the divergence of radiative heat flux used is for spectral radiant heat flux, but in order to keep everything manageable—computer timewise—an approximate two-band model is used. Absorption coefficients are computed by integrating over a 2371 line spectrum, stretching from 750 to 15,000 Å. The data for the 2371 line spectrum was obtained from Chul Park of NASA Ames. The absorption data for the

two-band model was found in the following way. At first for a representative temperature and density profile the heat load at the wall was computed[3] using the 2371 line absorption data. For this computation the expression in Eq. (3) was used. The same computation was repeated for the two-band model. By selecting different multipliers for this model the computations were repeated until the heat load at the wall agreed with that based on the exact 2371 line model. For the range of wavelengths, 750–2000-Å Rossland approximation was used for the absorption coefficients. For the range 2000–15,000-Å, Planck's approximation is used.

Results are obtained for two cases. The program is run with an adiabatic wall and a cooled wall. In both cases the code was run for a gray wall with different values of emissivity. For $\varepsilon = 0.08$ results are presented for a cooled wall and an adiabatic wall. The results for a cooled wall with emissivity, $\varepsilon = 0.7$ are also presented.

Fig. 2 shows the vector plot of the current density distribution in the electrode region for the case under consideration. It corresponds to an atmospheric arc with load current equal to 800 A. The current density is normalized by the quantity[1] (load current)/[$2\pi R$(electrode pitch)]. The electrode pitch for the cathode assembly under consideration is 3.2 cm. The larger the size of the arrows, the greater the current density. Initially, the current is concentrated near the axis, which is the core of the arc. The current is equally shared by the two electrodes, so that half the current terminates at each electrode. Beyond the second electrode, the current density distribution becomes insignificant. Figure 3 presents the temperature profile for a cathode region with a cold wall. The gas temperature near the wall is maintained constant at 3157 K. Radially the highest temperatures occur near the axis with magnitude decreasing in the direction of the flow. The reason for this could be that the arc is concentrated along the axis. Axially the temperatures are highest at the entrance of the electrode assembly and lowest at the exit. There are two factors that contribute to this. One is that all the current terminates at the electrodes so that the temperatures decrease in the direction of flow. The second reason is that radiative cooling occurs in the electrode region. Figure 4 shows the radiative heat flux corresponding to the temperature distribution of Fig. 3.

The results for an electrode region with adiabatic wall are shown in Figs. 5 and 6. In this case the temperature at the wall does not remain constant and is obtained as a converged solution. As for the cold wall, here too the temperatures at the entrance to the electrode assembly are the highest and decrease with the flow. This is true at the wall also. In the absence of cooling, the wall temperature reaches up to 10,960 K at the entrance. The temperature reduces to 3188 K at the end of the second insulator. In the vicinity of the axis and at the end of the electrode assembly the temperature distribution for the adiabatic and the cold wall are very close in magnitude. At the end of the electrode assembly the temperatures are low because all the arc current terminates at the two electrodes. The radiative flux profile for the adiabatic wall looks similar to the radiative profile for the cold wall. The only difference is that near the entrance the high flux region is more spread out in the axial direction.

Figures 7 and 8 illustrate the enthalpy distribution corresponding to the cold and adiabatic walls. It is normalized with respect to $\rho_\infty c_\infty^2$. In each case heat addition occurs due to the arc, consequently the enthalpy increases with the flow. The

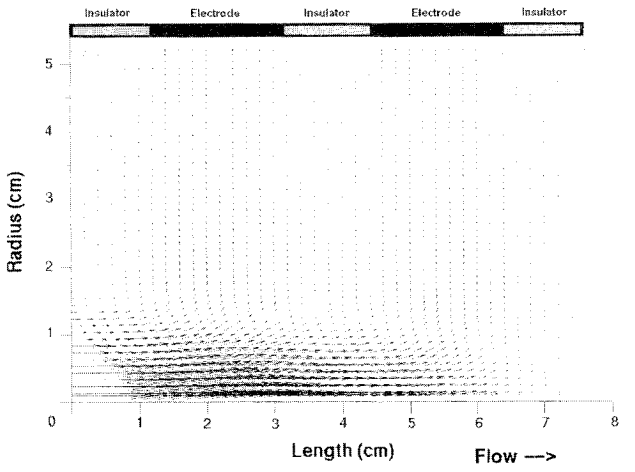


**Fig. 2 Current density distribution in the downstream cathode region for a two-electrode configuration. $I = 800$ A, $P = 1$ atm.**

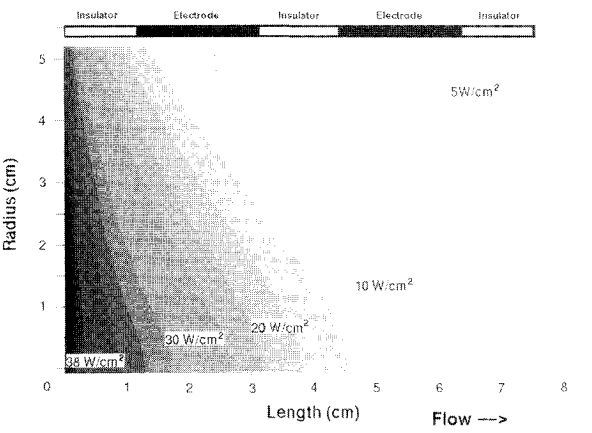


**Fig. 4 Radiant heat flux distribution for a cooled wall with $\varepsilon = 0.08$.**

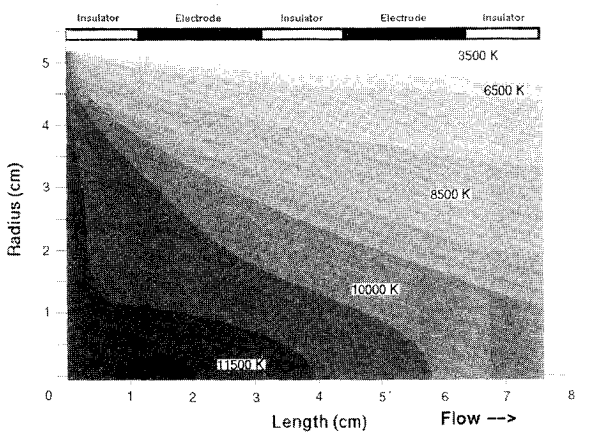


**Fig. 3 Temperature distribution for a cooled wall with $\varepsilon = 0.08$.**

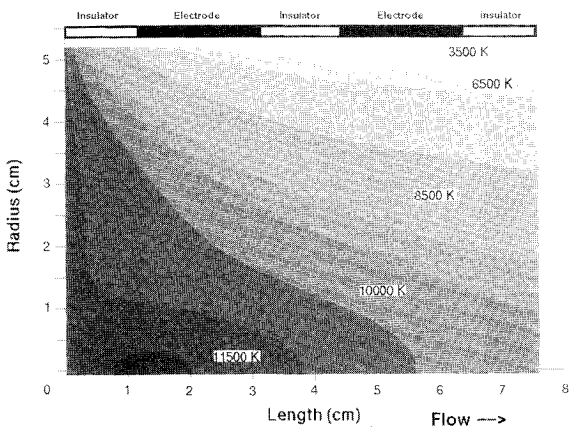


**Fig. 5 Temperature distribution for a adiabatic wall with $\varepsilon = 0.08$.**

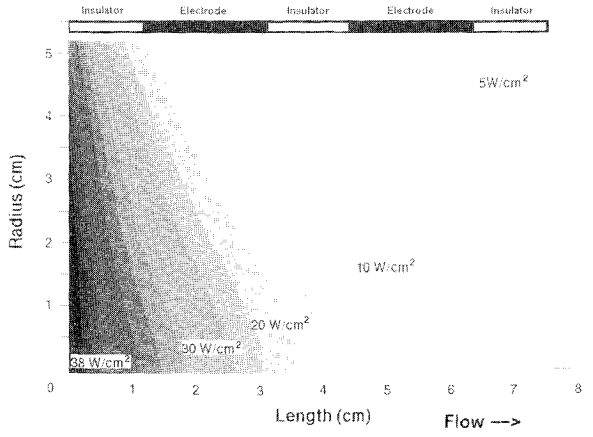


**Fig. 6 Radiant heat flux distribution for an adiabatic wall with $\varepsilon = 0.08$.**

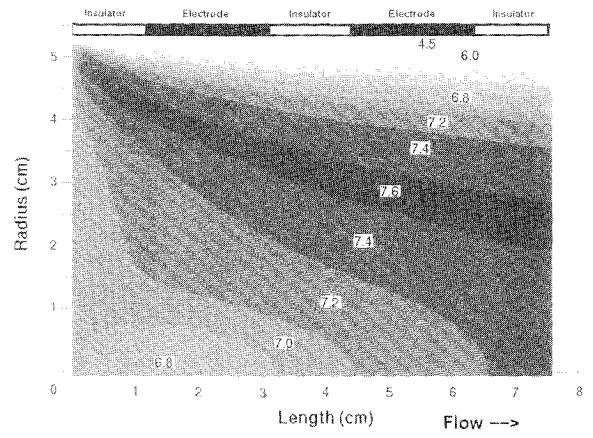


**Fig. 7 Enthalpy profile in the cathode region with cooled wall. $\varepsilon = 0.08$.**

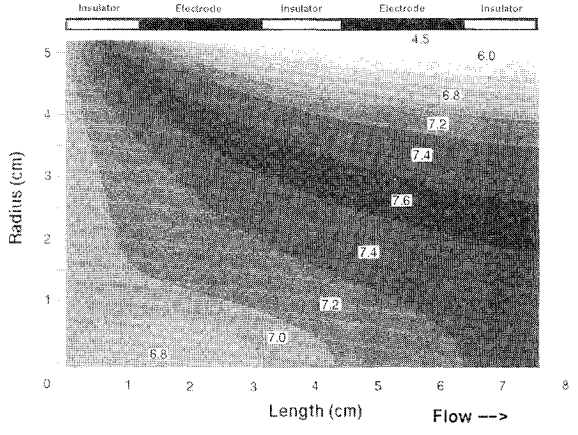


**Fig. 8 Enthalpy profile in the cathode region with adiabatic wall. $\varepsilon = 0.08$.**

difference in the two cases occurs near the wall. The reason for this is that in the case of the cold wall the temperature is maintained constant. At the end of the electrode assembly enthalpy starts to decrease. This is expected because beyond this region heat addition does not occur any more. The decrease in enthalpy is indicated by the change in the contours at the end of the electrode assembly. Although the enthalpy profile in the two cases is different near the wall, they seem to be very similar near the exit to the electrode assembly. This means that there is not much loss in enthalpy due to cooling of the wall.

The temperature, radiative heat flux, and enthalpy distribution for a cooled wall with $\varepsilon = 0.7$ are shown in Figs. 9–11. These should be compared with Figs. 3, 4, and 7. For a higher value of emissivity, more radiation is absorbed by the wall so that the radiation absorbed by the gas is less. This also leads to lower enthalpy for the gas.

Figure 12 illustrates the Joule heating in the electrode region. It is normalized with respect to $\rho_c c_c^2$. Most of it is concentrated in the vicinity of the electrode. The two peaks occur in the regions covered by the two electrodes. Each peak distinctly corresponds to the arc foot terminating at that partic-

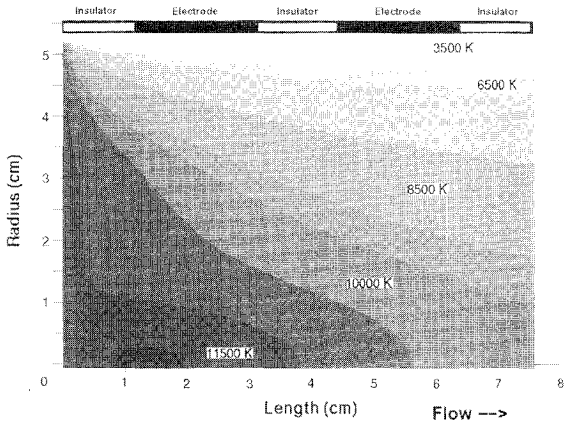


**Fig. 9 Temperature distribution for a cooled wall with $\varepsilon = 0.7$.**

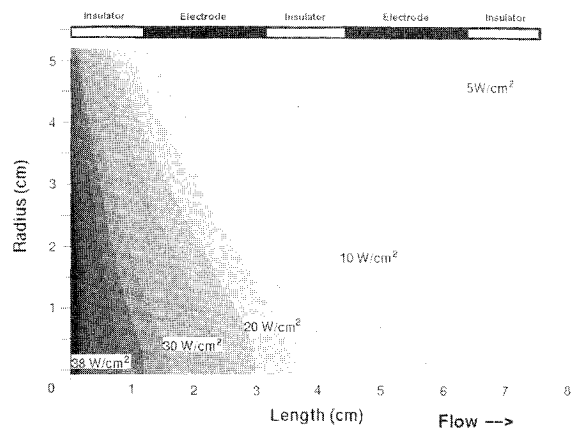


**Fig. 10 Radiant heat flux distribution for a cooled wall with $\varepsilon = 0.7$.**

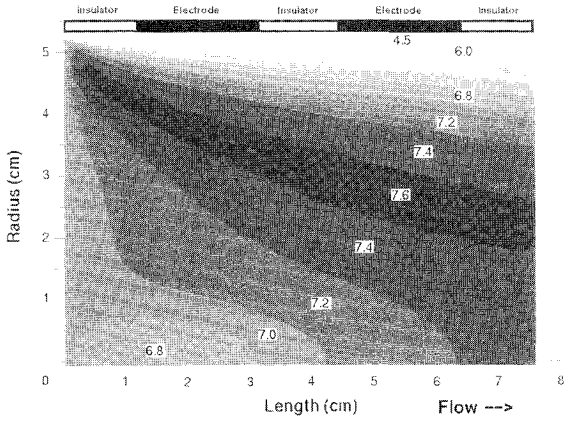


**Fig. 11 Enthalpy profile for a cooled wall with $\varepsilon = 0.7$.**

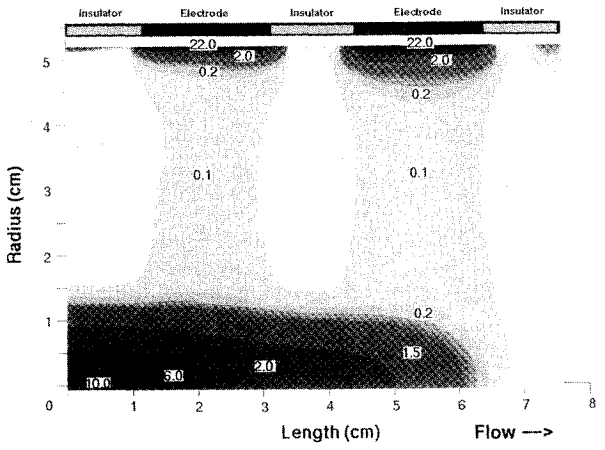


Fig. 12 Profile of Joule heating.

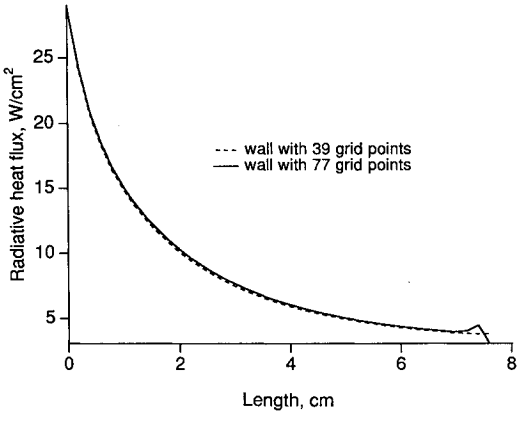


Fig. 13 Comparison of radiative heat load for adiabatic and cooled walls. $\varepsilon = 0.08$.

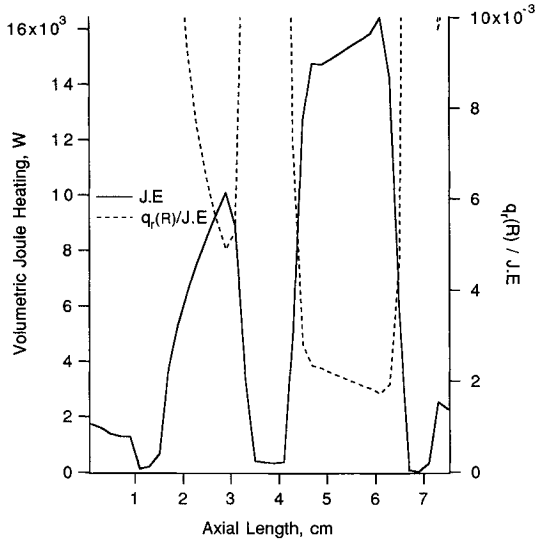


Fig. 14 Radiative heat load as a fraction of Joule heating.

ular electrode. Figure 13 compares the radiative heat flux along the wall for the two cases. It is observed that the radiative heat flux due to the adiabatic wall is slightly larger near the entrance and in the region covered by the first electrode. At the end of the second insulator and beyond, the radiative flux at the cold wall and the adiabatic wall are almost equal.

The radiative heat load at the wall as a fraction of Joules heating is shown in Fig. 14. For illustration the volumetric

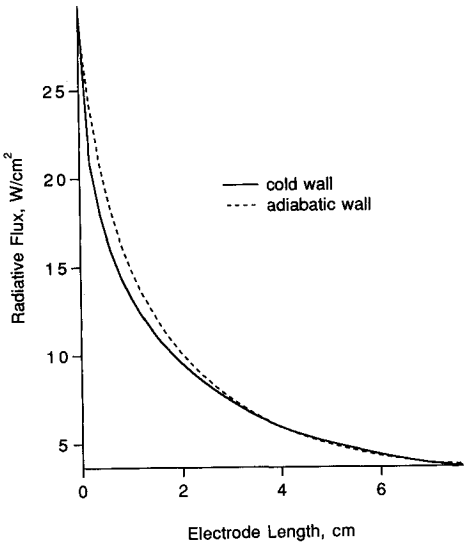


Fig. 15 Comparison of radiative heat flux for different grid sizes. $\varepsilon = 0.08$.

heat input ($j \cdot E \times$ volume) is also plotted in the figure. The figure shows that a larger fraction of $j \cdot E$ occurs at the second electrode. This is due to the fact that the second electrode is the terminating electrode and all the residual current has to terminate at this electrode. As expected, $j \cdot E$ at the insulators is small. At the wall, surface integral of $q_r(R)$ was performed. This represents the total heat load at the wall and comes out to be 2–6% of the total volumetric heat input into the gas. For high current, high-pressure devices, even 2–6% of the input energy can amount to significant heat load to the wall. At the insulator where the $j \cdot E$ term is very small, almost all the input energy is lost to radiation.

Computations are done on a Cray Y-MP C90. It is observed that a 39 × 39 grid axisymmetric problem with a two-band radiation model converges much faster for an adiabatic wall than for a cooled wall. It takes 2 h, 4 min of CPU time for convergence to occur for an adiabatic wall, and 2 h, 37 min of CPU time for a cooled wall. The additional CPU time used for the cooled wall can be attributed to the boundary condition that the temperature be maintained constant at the wall. In the current algorithm only the radiation term is strongly coupled. Radiation calculations consume 99% of the CPU time. Figure 15 compares the radiative heat flux at the wall computed with 39 × 39 grid points and 77 × 39 grid points. The reason for choosing a 77 × 39 grid is that it almost doubles the number of grid points along the wall where this comparison is made. Adiabatic boundary conditions are chosen because the run takes less computer time. The two sets of results differ by less than 5% everywhere except at the end of the electrode region. Therefore, it can be assumed that the results are not grid dependent.

## V. Conclusions

A subsonic fluid code is developed for the downstream electrode region. For a true axisymmetric geometry the radiation term has been strongly coupled successfully. A subsonic flowfield in chemical equilibrium is considered. Thermodynamic parameters are computed for the downstream cathode region. Computations are done for an adiabatic wall and a cooled wall. Of the two cases studied, convergence occurs faster with adiabatic boundary conditions at the wall. The code developed is grid independent.

This code made it possible to compute the heat load at the electrode surface for both an adiabatic and a cooled wall. In both cases it decreases in the direction of the flow. For adiabatic case the wall temperature rises as high as 10,960 K at

the entrance to the electrode assembly. It is observed that about 2–6% of input energy is transmitted to the wall by radiation. At present, experimental data for heat load at the electrode region is not available. Availability of such data would make it possible to validate this code and put more confidence in a future analysis.

## Acknowledgments

This work was supported by NASA Grant NCC-2-688 and NASA Contract NAS2-14031.

## References

[1]Durgapal, P., "Current Distribution in the Cathode Area of an Arc Heater," *Journal of Thermophysics and Heat Transfer*, Vol. 7, No. 2, 1993, pp. 241–250; also AIAA Paper 91-1385, June 1991.

[2]Durgapal, P., "Electrode Phenomena in High Current, High Pressure Arc Heaters," *Journal of Thermophysics and Heat Transfer*, Vol. 7, No. 3, 1993, pp. 412–417; also AIAA Paper 92-0810, Jan. 1992.

[3]Durgapal, P., "Radiative Transfer in the Electrode Region of an Arc Heater," AIAA Paper 92-2872, July 1992.

[4]Palmer, G. E., "Enhanced Thermochemical Nonequilibrium Computations of Flow Around the Aeroassist Flight Experiment Vehicle," AIAA Paper 90-1702, June 1990.

[5]Anderson, W. K., Thomas, J. L., and Van Leer, B., "Comparison of Finite Volume Flux Vector Splittings for the Euler Equations," *AIAA Journal*, Vol. 24, No. 9, 1986, pp. 1453–1460.

[6]Van Leer, B., "Towards the Ultimate Conservative Difference Scheme V: A Second-Order Sequel to Gudunov's Method," *Journal of Computational Physics*, Vol. 32, No. 1, 1979, pp. 101–136.